Reaction path model of the formation of abiotic immiscible hydrocarbon fluids in subducted carbonated serpentinites, Lanzo Massif (Western Italian Alps)

Abstract

Fluids generated from subducted slabs participate in the cycling of deep carbon in the crust and upper mantle. In these fluids, aqueous carbon species vary in oxidation state between +IV and -IV depending on whether the fluids are oxidizing or reducing, respectively. Most studies of subduction-zone fluids have focused on oxidized carbon species. However, recent studies of natural samples have demonstrated the occurrence of deep, reducing fluids, generated in both subducted oceanic upper mantle and crustal rocks. CH_4-H_2-rich fluid inclusions in subducted carbonated serpentinites have demonstrated the existence of abiotic, immiscible, hydrocarbon fluids at upper mantle conditions. To investigate the formation of such immiscible hydrocarbon fluids during the evolution of subducted carbonated serpentinites, we used equilibrium constants from the Deep Earth Water model to carry out predictive chemical mass transfer modeling to simulate the alteration reactions. A novel feature of the models was the inclusion of an immiscible hydrocarbon fluid containing six components ($CH_{4,f}, C_2H_{6,f}, C_3H_{8,f}, isoC_4H_{10,f}, CO_{2,f}, H_{2,f}$). This feature enabled prediction of the formation of a separate immiscible fluid in equilibrium with aqueous species and minerals.

We developed a predictive reaction path model of invasive $H_{2,f}$ reacting with carbonated serpentinites and interstitial aqueous fluids for comparison with the natural samples from the Lanzo Massif, western Italian Alps. Over a range of temperatures and pressures, immiscible hydrocarbon fluids formed in association with altered mineral assemblages. Reaction progress caused the transformation of carbonated serpentinites and the formation of clinopyroxene, brucite, graphite, and hydrocarbon fluids, along with changes of pH, $logf_{O_2}$, and aqueous species. $CH_{4,f}$ was the most abundant hydrocarbon species in all the models. The overall results at 2.0 GPa and

400 to 450 °C were consistent with the natural samples from the Lanzo Massif. Interestingly, large amounts of H_2O formed due to oxidation of H_2. More hydrocarbons and H_2O formed in models with lower fluid/rock mass ratios or with more reactant H_2. Models at different pressure and temperature conditions showed similar results with some variation in the relative stabilities of aragonite, graphite and olivine solid solution, and associated differences in mineral sequences, hydrocarbon fluids, values of aqueous species, and the final $logf_{O_2}$ and pH. Our models strongly support the laboratory and field evidence that reduction of carbonated serpentinites by infiltrating H_2 fluids can cause the formation of immiscible, abiotic hydrocarbon fluids in subduction zones.

Key words:

Abiotic hydrocarbon; Carbonated serpentinites; DEW model; Thermodynamic modeling; Deep carbon fluids

Highlights

- Novel reaction path model for invasive H_2 fluids interacting with carbonated serpentinites
- Use of the Deep Earth Water model for predictive chemical mass transfer modeling
- Significant immiscible CH_4 fluid and H_2O formed under high pressure and temperature
- Serpentinite and aragonite destroyed with brucite, graphite, and clinopyroxene formed
- Model results agree with natural samples from Lanzo Massif, western Italian Alps

1. Introduction

It has long been proposed that hydrocarbon fluids could exist in the deep Earth (Mendeleev 1877, Kudryavtsev 1959, Kolesnikov *et al.* 2009, 2017, Kutcherov and Krayushkin 2010). Although controversial (McCollom 2013, Sephton and Hazen 2013), a deep, abiotic theory for the origin of hydrocarbons received support in the late 20th century from the hypothesis of a deep hot biosphere feed by ascending abiotic fluid hydrocarbons from the deep Earth (Kudryavtsev 1951, Gold 1992, 2001). However, the amounts of abiotic hydrocarbons that could be produced in the upper mantle were never quantified and remain highly speculative.

Recent studies have suggested evidence of possible abiotic hydrocarbon-H_2-bearing fluids in association with ultramafic or mafic rocks and serpentinization in mid-ocean ridge settings where the hydrocarbons are present in minor quantities dissolved in the circulating aqueous fluids (Proskurowski *et al.* 2008, Alt *et al.* 2013, McDermott *et al.* 2015, Klein *et al.* 2019). However, it is doubtful that the CH_4 formed recently in the present hydrothermal circulation systems (McDermott *et al.* 2015, Reeves and Fiebig 2020). For example, Klein et al. (2019) suggested that H_2 and CH_4 can be formed inside olivine-hosted aqueous fluids as a result of host-inclusion interactions during cooling and subsequently released into the mid-ocean ridge hydrothermal circulation system.

Many fewer studies have been concerned with hydrocarbon production during high-pressure metamorphism in subduction zones, where most studies have typically focused on oxidized carbon species dissolved in the fluid phases (Hacker *et al.* 2003, Dasgupta and Hirschmann 2010, Scambelluri *et al.* 2019). Subduction zone serpentinization has been proposed to produce large amounts of H_2 and CH_4 (Vitale Brovarone *et al.* 2020). Additionally, CH_4 has

been found in high-pressure and ultra-high-pressure metabasic rocks (Tao *et al.* 2018, Zhu *et al.* 2020). Experimental and theoretical studies have demonstrated that H_2 and light hydrocarbons can be immiscible at subduction zone conditions (Huang et al., 2017; Huang et al., 2023; Li, 2017; Pruteanu et al., 2017). However, the generation of reduced-carbon species in subduction zone fluids or as immiscible phases has not received much attention. Nevertheless, natural confirmation of immiscible, CH_4-H_2-bearing fluids related to serpentinization in subduction zones have now been found world-wide. For example, coexisting aqueous and H_2-CH_4 -rich gaseous fluid inclusions in the Lanzo massif, western Italian Alps (Pelletier and Müntener 2006, Vitale Brovarone *et al.* 2017, 2020, Giuntoli *et al.* 2020, Sverjensky *et al.* 2020) have been suggested to document immiscibility of reduced fluids in metamorphic fluids. In these rocks, CH_4 formed by H_2-mediated reduction of carbonate in carbonated serpentinites. The reaction also resulted in the formation of diopside, brucite, graphite, ±Ca-rich garnet (Vitale Brovarone *et al.* 2017, Giuntoli *et al.* 2020). A recent geochronological study indicates that the event of CH_4 formation happened at peak metamorphic conditions (Piccoli *et al.* 2023), corresponding to about 500 °C and depths up to 80 km, or ~2.5 GPa (Vitale Brovarone et al., 2017 and references therein).

In addition to natural examples of abiotic hydrocarbons, numerous experimental studies of abiotic hydrocarbon formation at elevated temperatures and pressures have been reported (Foustoukos and Stern 2012, Manning *et al.* 2013, McCollom 2013). Under crustal conditions, the formation of hydrocarbons in serpentinization experiments has been widely studied with and without catalysts such as metallic iron (Barbier *et al.* 2020). At higher, upper mantle pressures, experimental studies have focused on fluids without minerals present. For example, immiscible CH_4-C_2H_6-H_2 fluid inclusions were recorded in quartz at 1.5 - 2.5 GPa and 600 - 700 °C (Li 2017), and immiscible hydrocarbon droplets containing isobutane and other hydrocarbons were observed

with *in situ* Raman spectroscopy at 1.6 – 4.6 GPa and 300° C (Huang et al., 2017; Huang et al., 2023).

Overall, natural examples and experiments at upper mantle temperatures and pressures indicate that the formation of immiscible abiotic hydrocarbons does occur. However, quantitative, predictive models of the formation of immiscible abiotic hydrocarbon fluids in geologic settings at depth have been lacking. In this study, we conducted predictive, irreversible chemical mass transfer modeling to simulate the formation of hydrocarbon fluids in a well-documented natural setting. We chose to model the reduction of carbonated serpentinites and the associated production of an immiscible CH_4-rich fluid in the Lanzo Massif previously described in detail by Vitale Brovarone et al. (2017). Following the genetic model by Vitale Brovarone et al. (2017), we modeled the interaction between H_2-rich fluids and carbonated serpentinites in the pressure and temperature range of 1.0 - 2.0 GPa and 400 - 500 °C which is consistent with reported subduction zone conditions (Van Keken *et al.* 2002, Syracuse *et al.* 2010, Penniston-Dorland *et al.* 2015, Holt and Condit 2021). Our models provide a test of our ability to predict the formation of immiscible hydrocarbon fluids in a chemically and mineralogically complex system at elevated pressure-temperature conditions for comparison with the observed mineral assemblages and fluid inclusion compositions previously described for the reduced carbonated serpentinites from the Lanzo Massif.

2. Geologic setting of the Lanzo Massif and abiotic methanogenesis during the reduction of carbonated serpentinites

The ultramafic rocks of the Lanzo Massif in the western Italian Alps underwent Cenozoic eclogite-facies peak metamorphic conditions to about 500-550 °C and 2 GPa (Rubatto and Hermann 2001, Pelletier and Müntener 2006). The massif includes carbonated serpentinites,

including carbonated serpentinites, regarded as the products of sub-seafloor hydrothermal reactions (Lagabrielle *et al.* 1990, Rubatto and Hermann 2001, Pelletier and Müntener 2006, Vitale Brovarone *et al.* 2017). The carbonated serpentinites are located in the pervasive serpentinized shell outside the peridotite core of the massif. The shell surrounds mostly the north and west sides of the peridotite core. For the purposes of the present study, the detailed petrographic, fluid inclusion, isotopic, modeling, and geochronological results reported by Vitale Brovarone et al. (2017), Giuntoli et al. (2020), and Piccoli et al. (2023) can be summarized by the following key points relevant to our reaction path modeling:

- The samples of carbonated serpentinite consist of clasts of serpentinite embedded in a Ca-carbonate matrix.
- Pristine serpentinite clasts consist mainly of antigorite – the serpentine mineral stable at high temperature and pressure conditions – and small amounts of chlorite and magnetite.
- The reacted serpentinite clasts are coated by ubiquitous graphite rims. Other product minerals include diopside ± brucite ± Ca-rich garnet ± perovskite ($CaTiO_3$).
- The reacted rocks are found along discrete layers within the carbonated serpentinite, which were interpreted as fluid pathways and shear zones (Giuntoli *et al.* 2020). Overall, the degree of alteration of the serpentinite clasts is highly variable on a spatial scale of meters.
- Petrographic relations indicate that graphite formation occurred at high-pressure conditions in the antigorite stability field. Dating of syn-reduction perovskite including CH_4 and graphite inclusions provided an age of 49.6 ± 1 Ma (Piccoli *et al.* 2023), which is consistent with previous constraints on the peak metamorphic age of the Lanzo massif (Rubatto and Hermann, 2001).

- Two types of structurally coexisting fluid inclusion populations were found in the carbonate matrix adjacent to serpentinite clasts and the reacted rims of serpentinite: a CH_4-H_2-rich population and a H_2O-rich population. These two populations were interpreted to represent coexisting immiscible fluids (Vitale Brovarone *et al.* 2017, Sverjensky *et al.* 2020).
- The $\delta^{13}C$ values of the residual, reacted carbonate samples are up to about 8 per mil heavier than the least reacted samples which have typical marine carbonate values of about 2 - 3 per mil relative to the PeeDee Belemnite standard (Vitale Brovarone *et al.* 2017). These values are consistent with the partial transformation of carbonate into CH_4.
- The CH_4 genesis was interpreted as the result of H_2-carbonate interactions along channelized fluid pathways inside the carbonated seprentinite. The process was summarized according to the following overall reaction:

$$antigorite + 17Ca\text{-}carbonate + 68H_2 = 17diopside + 31brucite + 17CH_4 + 34H_2O \quad (1)$$

$$Mg_{48}Si_{34}O_{85}(OH)_{62} + 17CaCO_3 + 68H_2 = 17CaMgSi_2O_6 + 31Mg(OH)_2 + 17CH_4 + 34H_2O \quad (2)$$

- Overall, the mineral assemblages and fluid inclusions suggest the reduction of carbon in Ca-carbonate by the H_2-fluids to form CH_4 and graphite. Reaction between the external H_2 and the newly formed graphite was also proposed to generate additional CH_4.
- The pressure and temperature conditions of the reactions were determined by the presence of graphite and aragonite inclusions in magnetite, and syn-reduction antigorite, and modeled in a simplified $Ca\text{-}Mg\text{-}Si\text{-}C\text{-}O\text{-}H$ thermodynamic system. The minimum condition was inferred to be 1.0 GPa and 370 °C (i.e., 370 $°C\ GPa^{-1}$ of gradient, same as

below) constrained by graphite-aragonite coexistence along the exhumation path of the Lanzo massif. The maximum condition was predicted to be about 2.5 GPa and 500 °C (200 $°C\ GPa^{-1}$) constrained by the peak metamorphic condition of the Lanzo Massif.

- The oxygen fugacities during the reactions were estimated to range from log f_{O_2} -29 to -37 (QFM -3 to -6), assuming graphite saturation and the co-occurrence of magnetite in the carbonated serpentinites.

3. Methods

3.1 Thermodynamic data for aqueous species and minerals

We have used the geochemical Deep Earth Water (DEW) model which was built to address the predictive geochemical modeling challenge of a huge range of temperatures, pressures, and chemically complex systems (Sverjensky *et al.* 2014, Huang and Sverjensky 2019, Sverjensky 2019). The DEW model is based on predictive geochemical theory resting on decades of theoretical and experimental studies of the thermodynamic properties of electrolytes, neutral aqueous solutes, metal-complexes, and organic species. The DEW model enables prediction of equilibrium constants involving aqueous species of all types to be incorporated into the data files for aqueous speciation, solubility, and chemical mass transfer codes. Here we use the codes EQ3 & EQ6 (Wolery 1992) modified to operate at elevated temperatures and pressures. The standard Gibbs free energies of formation of the end-member mineral components were calculated with the modified Berman thermodynamic database (Berman 1988, Sverjensky *et al.* 1991, Sverjensky 2019).

3.2 Standard Gibbs free energies of fluid H_2 and CO_2

The calculation of chemical mass transfer involving immiscible hydrocarbon fluids requires the computation of standard Gibbs free energies of the pure end-member hydrocarbon species as well as other pure fluid species that are relevant to the modeling described below. Here we made use of six organic and inorganic pure fluid species, all of which are relevant to this study. These fluid species include the following: methane ($CH_{4,f}$), ethane ($C_2H_{6,f}$), propane ($C_3H_{8,f}$), isobutane ($isoC_4H_{10,f}$), carbon dioxide ($CO_{2,f}$), and hydrogen ($H_{2,f}$) where the subscript f refers to the supercritical fluid compound. The apparent standard Gibbs free energies of formation ($\Delta G^0_{f;T,P}$) of these species are given in the Appendix A. They were obtained by first calculating the $\Delta G^0_{f;T,P^0}$ of the pure gas, then the fugacity coefficients (ϕ) were obtained from the GFluids spreadsheet (Zhang and Duan 2010) at 1.0 - 5.0 GPa and 300 - 650 °C (values below 400 °C were extrapolated to 300 °C using the data from the higher temperatures). Equilibrium constants involving these species and aqueous species were calculated using the DEW model and incorporated into the data files for the codes EQ3 and EQ6.

3.3 Incorporation of hydrocarbon fluids in aqueous speciation, solubility, and chemical mass transfer models

Although aqueous C-species of many types in the spectrum of inorganic to organic species have long been used in aqueous speciation, solubility, and chemical mass transfer models, immiscible inorganic or organic fluids have not been used in such models. Here, we incorporated such species using a number of approximations. Mathematically, this incorporation can be done by including the predicted $logK$ values for equilibrium between any potentially immiscible fluid

156 species (e.g. $H_{2,f}$ or $CH_{4,f}$) and a strict basis species into the thermodynamic data file as a "mineral
157 species". For example, we decided to put fluid methane ($CH_{4,f}$) into the datafile of EQ3 and EQ6
158 using the equilibrium

159 $$CH_{4,f} + 2O_{2,g} = CO_3^{2-} + 2H^+ + H_2 \quad (3)$$

160 During model calculations, the above equilibrium enables the fluid species to reach
161 saturation and "precipitate" as a pure fluid phase immiscible with the aqueous fluid and any
162 minerals in equilibrium with the aqueous fluid according to the reaction

163 $$CH_{4,aq}^0 = CH_{4,f} \quad (4)$$

164 Examples of reactions such as Eq. (4), which are just solubility reactions, are discussed below as
165 functions of temperature and pressure.

166 Building on the above, two or more such potentially immiscible fluid species can be entered
167 as potential components of a "solid-solution" in the data file of the codes EQ3 and EQ6, which
168 enables formation of an immiscible fluid phase (e.g., a hydrocarbon fluid phase containing
169 multiple hydrocarbon components). In the present study, the end-member components of the
170 immiscible hydrocarbon fluid were assumed to mix ideally. At elevated temperatures and pressures,
171 this is a major assumption. However, in almost all our model results the hydrocarbon fluid that
172 formed was greater than 90% fluid CH_4. Therefore, as a first approximation, it seems reasonable
173 to assume ideal mixing in the hydrocarbon fluid.

174 ***3.4 Conceptual model and assumptions for chemical mass transfer calculations***

175 As discussed above, the carbonated serpentinite of interest consisted of clasts of
176 serpentinite embedded in an aragonite matrix. The serpentinite is composed mainly of antigorite
177 with minor magnetite and chlorite. We assume here a conceptual model in which an external H_2
178 fluid invades and reacts with the carbonated serpentinite assemblages that contain some interstitial

aqueous fluid. As a first approximation, the composition of this initial interstitial fluid was assumed to be determined by equilibrium with the rock minerals. Using the aqueous speciation and solubility code EQ3 (Wolery 1992), the concentrations of the elements Ca, Si, Fe, and Al, were determined by equilibrium with aragonite, antigorite, magnetite, and the clinochlore component of a chlorite solid solution (X_{Mg} 0.97), respectively. Mg was set to a value below the saturation of brucite. Na and Cl were set to low values of 0.001 m as the salinity of the aqueous fluid predating the reactions is not known. C was set to a small value, e.g. $\leq$ 0.1 molal, in equilibrium with aragonite, so the amount of aqueous C is not important in the initial fluid. Either Na^+ or H^+ was determined by charge balance leading to a calculated value of the pH. Wide ranges of the initial value of the $logf_{O_2}$ were tested. Optimal values were selected based on the constraints of minimizing the initial aqueous carbon concentration in equilibrium with aragonite such that the computed aqueous Ca concentrations were not so high as to result in supersaturation of the initial fluid with respect to diopside or clinopyroxene solid solution. These constraints typically resulted in $logf_{O_2}$ values of QFM to QFM - 2. As an example, the bulk composition and most abundant C-species and fluid properties of an initial fluid at 400°C and 2.0 GPa are listed in Table 1 where it can be seen that the $logf_{O_2}$ is equal to QFM-1.3.

The initial aqueous fluids were subsequently used as input to the chemical mass transfer code (EQ6), together with the carbonated serpentinite reactant minerals and external H_2 fluid reactant. The Lanzo carbonated serpentinite was approximated by 15 vol% of aragonite and 85 vol% of serpentinite. The serpentinite contained 96.5 vol% of antigorite, 1.0 vol% of magnetite, and 2.5 vol% of chlorite. This assumption of a standard run provides an example of the composition of the carbonated serpentinites. Additional models were considered for higher aragonite/serpentinite ratios (Appendix A). To explore the effect of variable fluid-rock (F/R) ratio,

the total amount of reactant rocks was varied from 669 g to 10,000 g per 1,000 g of H_2O in the initial aqueous fluid. The initial amount of reactant H_2 in moles per 1,000 g of H_2O was determined by the need to overwhelm the redox buffering capacity of the initial rock in order to form hydrocarbon fluid. Within the framework of the assumptions adopted above, numerous reaction path models were run to explore variable temperatures, pressures, initial oxidation states, and F/R ratios. A representative set of these is included in the Supplementary Materials. The overall goal was to compare the predicted model outputs to the mineral assemblages in the rocks and the hydrocarbon fluids recorded in fluid inclusions reported for the Lanzo Massif by Vitale Brovarone et al. (2017) and Giuntoli et al. (2020).

4. Results

4.1 Predicted equilibria between fluid hydrocarbons, aqueous C-species, and graphite at upper mantle conditions

4.1.1 Predicted equilibria between pure immiscible fluids and aqueous species

Either H_2O-bearing and CH_4-H_2 fluids were observed in microstructurally coexisting fluid inclusions populations of the Lanzo reduced carbonated serpentinite, suggesting at least two types of immiscible fluids could appear in the natural samples. Accordingly, a number of fluid phases, including hydrocarbon and inorganic species at upper mantle conditions were incorporated in our model. The values of the equilibrium constants were predicted using the DEW model (Sverjensky *et al.* 2014) adapted for equilibria between pure fluid and aqueous species. The standard states for the fluid species $CH_{4,f}$, $C_2H_{6,f}$, $CO_{2,f}$, and $H_{2,f}$ were chosen to be the pure fluids at the temperatures and pressures of interest. Equilibria between such fluids and the corresponding

223 aqueous species represent the maximum activities of the aqueous species, i.e. the solubility of the
224 pure fluid component as an aqueous species.

225 The predicted $logK$ values displayed in Figs. 1A - D cover a wide range of temperatures
226 and pressures from 300 - 650 °C and 0.5 - 5.0 GPa. It can be seen in the figures that, overall, the
227 $logK$ values increased with temperature and decreased with pressure, with some exceptions at 0.5
228 - 1.0 GPa. In another words, the solubilities of fluid $CH_{4,f}$, $C_2H_{6,f}$, $CO_{2,f}$, and $H_{2,f}$ in aqueous
229 solutions increase with temperature but decrease with pressures greater than about 1.5 GPa. At
230 temperatures between 400 and 500 °C, the solubilities decrease in the order: $CH_4 < C_2H_6 < H_2 <$
231 CO_2. As a first order generalization, it should therefore be easier to form immiscible CH_4-rich
232 fluids than any of the others.

233 Although the equilibria shown in Figs. 1A-D are fundamental to the formation of
234 immiscible fluids, other factors also may exert a strong influence. Clearly, the redox state of a
235 system is extremely important. For example, if the $logf_{O_2}$ is low enough, the formation of a CH_4
236 -rich fluid will be strongly favoured relative to the other C-species. This tendency can be expected
237 to be magnified when the H_2 is continuously added and reacted with minerals. Furthermore, the
238 equilibria between aqueous and fluid species depends on $logf_{O_2}$, pH, total C content and other
239 features of the system. Different results could occur with a wider range of conditions beyond the
240 scope of this work.

241 *4.1.2 Predicted equilibria between pure fluid methane, aqueous methane, and graphite*

242 Graphite was an important product in the Lanzo reduced carbonated serpentinite and was
243 observed to be closely related to the CH_4-H_2 fluid inclusions (Vitale Brovarone *et al.* 2017). In
244 Fig. 2, the stability fields of aqueous CH_4, pure fluid CH_4 ($CH_{4,f}$) and graphite were plotted as

functions of $logf_{O_2}$ and $\log a_{CH^0_{4,aq}}$ at 1.0 - 2.0 GPa and 400 - 500 °C (Fig. 2). The equilibrium between aqueous and fluid CH_4 is determined solely by the equilibrium in Fig. 1A. It can be seen that the predicted $\log a_{CH^0_{4,aq}}$ in equilibrium with $CH_{4,f}$ range from 0.4 to 1.1 in Figs. 2A -D. The activity coefficient of $\log a_{CH^0_{4,aq}}$ was assumed to be unity in our subsequent modeling. As expected from Fig. 1A, the stability field of $CH_{4,f}$ expanded against $CH^0_{4,aq}$ at lower temperature and higher pressure.

The equilibrium between fluid $CH_{4,f}$ and graphite can be expressed in terms of $logf_{O_2}$ by writing the reaction

$$Graphite + 2H_2O = O_{2,g} + CH^0_{4,aq} \quad (5)$$

From which the $logf_{O_2}$ can be expressed by the $logK$ of Eq. (5) and $\log a_{CH^0_{4,aq}}$ as

$$logf_{O_2} = -loga_{CH^0_{4,aq}} + logK \quad (6)$$

assuming that a_{H_2O} is unity. In Figs. 2A - D, this equilibrium is expressed as a line with a slope of -1.0 and intersecting the line representing equilibrium between $CH_{4,f}$ and $CH^0_{4,aq}$ at an invariant point. It can also be seen that the equilibrium between fluid CH_4 and graphite is about 3.0 log units below the QFM buffer, in agreement with the prediction by Vitale Brovarone et al. (2017). We also included the magnetite-α-Fe buffer, and the H_2O-$H_{2,f}$ buffers with $a_{H_{2,f}}$ of 0.1 and 1.0. These buffers all plot in the $CH_{4,aq}$ and $CH_{4,f}$ fields.

The phase diagrams in Figs. 2A - D provided guidance for setting up the initial $logf_{O_2}$ of our model aqueous fluid resulting in values above the $CH^0_{4,aq}$ field and amounts of initial carbon lower than saturation with graphite or $CH_{4,f}$. Starting from these conditions, when $logf_{O_2}$ decreases, and when $CH^0_{4,aq}$ increases, the figures show that it can be expected that the boundary

of $CH^0_{4,aq}$ and $CH_{4,f}$ will be reached, followed by the stability field of CH_4-rich hydrocarbon fluid.

It should be noted here that although graphite appears as a phase in Figs. 2A - D, these figures refer to a chemical system without the component CaO, an important component in the natural carbonated serpentinites. When CaO is included, the stability of graphite is limited by the appearance of aragonite or calcite solid solution, depending on the value of the $log\left({a_{Ca^{2+}}}/{(a_{H^+})^2}\right)$ in the aqueous phase. For the conditions we modeled below, the stability field of graphite is replaced by aragonite or calcite solid solution at 1.0 GPa and 400°C.

4.2 Fluid hydrocarbon formation during the destruction of carbonated serpentinites in the Lanzo Massif

Chemical mass transfer models of the transformation of carbonated serpentinites by H_2 fluids were conducted at 1.0 - 2.0 GPa and 400 °C - 500 °C consistent with the conditions proposed for the Lanzo Massif (Vitale Brovarone *et al.* 2017). The initial aqueous fluids were predicted at each pressure and temperature condition (Table 1, S-1, S-2, S-3, S-4) using an aqueous speciation solubility model as described above (section 3.3). The initial total concentrations of the aqueous carbon were 0.01, 0.05, or 0.1 molal, which were the lowest values usable given our assumptions about equilibrium with the minerals and with initial $logf_{O_2}$ values between QFM -1.6 to +1.2. The saturation activity of $CH^0_{4,aq}$ increased with temperature at the same pressure. The carbon speciation in the initial fluids was controlled by $logf_{O_2}$ relative to the QFM buffer and the total aqueous carbon concentrations. For example, at 1.5 GPa and 400 °C, two oxidation states could be considered: at $logf_{O_2}$ of QFM+1.0, $CH_{4,aq}$ is 0.03% of the total carbon of 0.01 m, whereas at

288 $logf_{O_2}$ of QFM-1.4, $CH_{4,aq}$ is 91.4% of the total carbon of 0.1 m. Importantly, the different
289 oxidation states of these two fluids did not affect the major results of the mass transfer reactions.
290 Therefore, either fluid could be used at each pressure and temperature. In other words, the initial
291 values of $logf_{O_2}$ in the fluid were not important variables. The main reason being that in all cases
292 the total initial carbon in the fluid was low.

293 *4.2.1 The standard model at 2.0 GPa and 400.0 °C and F/R equal to 0.1*

294 Here we present a mass transfer model at 2.0 GPa and 400 °C and F/R equal to 1.0 that
295 can serve as a representative example of our modeling (Table 1, Fig. 3). At this temperature and
296 pressure, the activity of $CH^0_{4,aq}$ in equilibrium with pure methane fluid was 2.4 (see Fig. 1A).
297 Therefore, as the aqueous activity coefficient in our model for neutral species was assumed to be
298 unity, at least 2.4 m $CH^0_{4,aq}$ would need to accumulate in the fluid during the mass transfer
299 reactions for an immiscible pure methane fluid to form. In our models, a hydrocarbon fluid with
300 variable composition could form. Such a fluid was more stable than a pure methane fluid; therefore,
301 it could form at concentrations of C less than 2.4 m. The initial mineral reactants were 16.45 moles
302 of aragonite, 3.53 moles of antigorite, 0.71 moles of magnetite, and 1.88 moles of chlorite(ss) per
303 1,000 g of H_2O. The initial aqueous fluid/rock (F/R) mass ratio was 0.10. This ratio was the lowest
304 value tested and corresponded to 10.0 kg of rock and of a dilute initial aqueous fluid containing
305 1.0 kg of H_2O. The endpoint of the model was determined by the initial amount of H_2 with a value
306 of 66.5 moles per 1000 g of H_2O (Table 2). This value of H_2 resulted in the formation of
307 hydrocarbon fluids without secondary olivine(ss) appearance due to the reduction of magnetite.
308 The initial and final aqueous fluid compositions and mineral assemblages are shown in
309 Table 1 and the detailed mass transfer results are shown as a function of the logarithm of the

reaction progress ($log\ \xi$) in Figs. 3A - E. Here, ξ represents the number of moles of H_2 added. The full reaction path output file is given in Appendix A. It can be seen in Fig. 3A that the reactant minerals, aragonite, antigorite, and magnetite were stable in the beginning, as these were used in the EQ3 code to develop the initial aqueous fluid chemistry, while chlorite(ss) increased with $log\ \xi$. At a $log\ \xi$ value of -1.37, clinopyroxene(ss) appeared consisting of almost pure diopside (95%) and miner hedenbergite (5%). The mole fraction of diopside decreased slightly to 90% until the end of the reaction (Table 1). Chlorite(ss) reached a plateau after $log\ \xi$ of 0.28. Shortly after, brucite started to form, then antigorite and aragonite decreased strongly. Graphite then formed and increased until aragonite was totally destroyed; meanwhile, antigorite stopped decreasing. The graphitization could be expressed as the following reaction:

$$antigorite + 17Ca\text{-}carbonate + 34H_2 = 17diopside + 31brucite + 17graphite \quad (7)$$

$$Mg_{48}Si_{34}O_{85}(OH)_{62} + 17CaCO_3 + 34H_2 = 17CaMgSi_2O_6 + 31Mg(OH)_2 + 17C + 34H_2O \quad (8)$$

Finally, hydrocarbon fluid formed and completed replaced graphite. This reaction could be expressed as the reaction below:

$$graphite + 2H_{2,f} \rightarrow CH_{4,f} \quad (9)$$

The overall reaction of methane genesis was presented in Eqs. (1 and 2). The hydrocarbon fluid contained almost pure $CH_{4,f}$ (99.7%), as well as $C_2H_{6,f}$ (0.1%), $H_{2,f}$ (0.2%). Only trace amounts of $C_3H_{8,f}$ and $isoC_4H_{10,f}$ were produced. The amount of hydrocarbon fluid increased mainly during the final period of reaction progress ($\Delta log\ \xi$ 0.21).

The change of mineral volumes can be seen in Fig. 3B. The volumes shown refer to 25°C and 0.1 MPa but these differ by less than about 3% from the volumes at 400°C and 2.0 GPa. For

333 the model system volume of in a 4,600 cm^3 (3,800 cm^3 of reactant rock and 800 cm^3 of initial
334 aqueous fluid), the volumes show a dramatic destruction of antigorite and aragonite by about 1,680
335 cm^3 and 560 cm^3, respectively, while the other two reactants (magnetite and chlorite) were just
336 accessory minerals. In terms of product minerals, about ~1,090 cm^3 of clinopyroxene(ss) and
337 ~770 $cm^3$of brucite were generated. Despite the significant number of moles of graphite formed,
338 the volume of graphite is small. The total volume of product minerals was about ~380 cm^3 less
339 than the destroyed reactants. However, in addition to the mineral products, about 32.3 moles of
340 H_2O and 12.7 moles of fluid CH_4 were also produced (Table 2), which corresponded to about 487
341 cm^3 of H_2O and 332 cm^3 of fluid CH_4, respectively (see also Fig. 4B below). Overall, the volume
342 of the system expanded by around 440 cm^3. The reactions are self-promoting because more fluid
343 CH_4 formed at 2.0 GPa and 400 °C than lower pressures (Fig. 6A, see section 4.2.3).

344 The molalities of most dissolved elements showed only small changes as a function of
345 $log\ \xi$ (Fig. 3C). Ca increased slowly and then decreased a little in the end. Fe decreased because
346 of the formation of clinopyroxene(ss). Then after clinopyroxene(ss) reached a peak, the reduction
347 of magnetite caused the decrease of Fe. Na, Cl, and Al did not participate significantly in any
348 reactions. However, the total dissolved C increased strongly with $log\ \xi$ as aragonite progressively
349 dissolved. The molality of C reached a plateau when graphite formed, and the system was buffered.

350 Major changes in $logf_{O_2}$ and pH can be seen in Fig. 3D. The values of $logf_{O_2}$ decreased
351 gradually then strongly, corresponding to the continuous addition of H_2 as a function of $log\ \xi$. A
352 plateau was reached when graphite appeared, which buffered the $logf_{O_2}$ co-existing with aragonite.
353 After all the aragonite was destroyed, the $logf_{O_2}$ dropped quickly to the value where graphite and
354 hydrocarbon fluids (almost pure $CH_{4,f}$) could co-exist. The final $logf_{O_2}$ was -30.2 (QFM -4.1).

The initial pH was very alkaline with significant amounts of Ca and Mg (Table 1). Overall, it was a $Mg(OH)_2$ and $Ca(OH)_2$ solution. Interestingly, the pH became even more alkaline with $log\ \xi$ as more Ca was added to the fluid by dissolution of aragonite (Fig. 3D). The rate of increase slowed when clinopyroxene(ss) appeared, and then reached a peak after brucite appeared, resulting in buffering of the pH at 5.80. The pH decreased a little to 5.77 corresponding to the formation of the hydrocarbon fluids.

The change of concentrations of individual aqueous species mirrors the above changes in the $logf_{O_2}$, pH, and mineral products (Fig. 3E). It can be seen that $CH^0_{4,aq}$ was the most abundant aqueous C-species and increased until graphite formed after which it increased again. These changes correspond to the conversion of the carbonate in aragonite to graphite and then to methane. The trends of the other aqueous hydrocarbon species were similar. Carbonate species decreased all the way because of the drop of $logf_{O_2}$. The molality of $H^0_{2,aq}$ did not increase much until the last stage of the reaction progress where it only reached about 10 millimolal, which means that almost all the reactant H_2 were consumed by incorporation into hydrocarbons as well as oxidation to H_2O and OH-groups in brucite.

4.2.2 Models at 2.0 GPa and 400 °C with different initial F/R mass ratios

The standard model discussed above referred to an initial F/R ratio of 0.10 by weight. In that model, the initial mass of rock was 10.0 kg and the initial fluid contained 1.0 kg H_2O (55.51 moles). We also investigated models with higher initial F/R for two reasons. First, the F/R of natural samples are variable, and we could test differences in the model results if the decarbonation reactions were extended. Second, higher F/R ratios might represent initial carbonated serpentinites with a higher porosity. Third, higher F/R ratios imply less amounts of initial

377 aragonite relative to 1.0 kg H_2O, which in turn requires less H_2 to destroy the aragonite and
378 facilitate the formation of hydrocarbon fluids.

379 Models of four additional initial F/R ratios were calculated ranging from 0.10 to 0.63 and
380 corresponding initial amounts of reactant H_2 from 66.5 moles to 10.6 moles, respectively (Table 2
381 and Figs. 4A and B). All the models finished before the formation of olivine(ss). The mass ratios
382 of H_2 and rock were very similar for all the runs, around 0.0133 (Table 2 and Fig. 4A).
383 Interestingly, even with a wide range of F/R ratios, the predicted mineral sequences, solid solution
384 compositions, hydrocarbon fluid compositions, $logf_{O_2}$, pH, trends of dissolved elements and
385 aqueous species were all very similar to the standard run described above. The absolute amounts
386 of minerals and hydrocarbon fluids decreased with higher F/R ratios. Less H_2O formed during the
387 reactions (from 32.3 to 5.57 moles) so the concentration of elements and aqueous species were
388 lower than the standard run (Fig. 4B).

389 The formation of hydrocarbon fluids decreased by 2 log units corresponding to the rise in
390 F/R from 0.10 to 0.63 (Table 2, Fig. 4B). The mass of rock after reaction decreased in every run.
391 In the standard run, the mass of rock decreased by 7.30%. The percentage of decrease was slightly
392 greater in runs with higher F/R (8.18%). Taking into account the final amounts of H_2O, the final
393 values of F/R could be calculated, and they were higher than the initial F/R ratio because of the
394 significant number of moles of excess H_2O created during the mass transfer. The percentage of
395 increase was 10% for the initial F/R ratio of 0.63, but reached 59% for the initial F/R ratio of
396 0.10. To conclude, lowering the F/R increased the formation of the immiscible hydrocarbon fluids
397 significantly because of the reduction of large amounts of aragonite. Because of the extra H_2O
398 formed, the aqueous fluids were diluted by the oxidation of H_2 fluids and $CH^0_{4,aq}$ was the only
399 major aqueous carbon species.

400 *4.2.3 Models at different temperature-pressure conditions*

401 To investigate the roles of temperature and pressure during the formation of hydrocarbons
402 from the reduction of carbonated serpentinite, we expanded our conceptual model at pressure and
403 temperature conditions along the metamorphic path of the Lanzo Massif (Vitale Brovarone *et al.*
404 2017, Giuntoli *et al.* 2020). The pressure and temperature conditions run with the mass transfer
405 model were 1.0 GPa and 400 °C, 1.5 GPa and 400 °C, 2.0 GPa and 450 °C, and 2.0 GPa and 500 °C
406 (Figs. 5, 6, & 7, Table S-1 to S-4) with a F/R mass ratio of 0.1. The rock reactants were the same
407 for each run: 16.45 moles of aragonite, 3.53 moles of antigorite, 0.71 moles of magnetite, and 1.88
408 moles of chlorite(ss). However, the numbers of moles of H_2 needed were 68.4, 66.4, 53.9, and
409 76.8, respectively, depending on the reaction conditions. At 1.5 GPa and 400 °C, the amount of
410 H_2 corresponds to the point just before olivine(ss) formation, the same as the standard run at 2.0
411 GPa and 400 °C. However, at 1.0 GPa and 400 °C, 2.0 GPa and 450 °C, and 2.0 GPa and 500 °C,
412 the number of moles of H_2 corresponds to the point when 1.0 mole of hydrocarbon fluids formed
413 because olivine(ss) formed before hydrocarbon fluids.

414 The lowest pressure considered, 1.0 GPa and 400 °C, was on the exhumation path, other
415 conditions were on the prograde path of the Lanzo massif (Vitale Brovarone *et al.* 2017). Figure 5
416 presents the amounts of minerals, both reactants and products, as a function of $log\ \xi$. Antigorite
417 was stable in the beginning and then decreased at all conditions. Because of the large molecular
418 formula of antigorite, the destroyed volume of antigorite reached about 1,800 cm^3 (37% of the
419 total volume in the system). Clinopyroxene(ss) was the first product mineral with almost pure
420 diopside and then brucite formed in all the runs. Chlorite(ss) with more than 95 mol% clinochlore
421 did not react and stayed until the end of the runs, except for a slight decrease at 1.0 GPa and 400 °C.
422 Hydrocarbon fluids formed during a late interval of reaction progress and increased quickly.

423 At 1.0 GPa and 400 °C, calcite(ss) was more stable than aragonite (Fig. 5A, Table S-1).
424 Interestingly, this, the retrograde path model, was the only model without graphite formation.
425 Hydrocarbon fluids formed directly from calcite(ss). As mentioned above, graphite is not stable
426 relative to aragonite for certain levels of the ratio $a_{Ca^{2+}}/a_{H^+}^2$ in the aqueous phase. At this pressure
427 and temperature, graphite cannot be stable when the aqueous fluid has a $\log(a_{Ca^{2+}}/a_{H^+}^2)$ value
428 less than 9.50. In the run shown in Fig. 5A, the value of $\log(a_{Ca^{2+}}/a_{H^+}^2)$ changed from an initial
429 value of 9.29 to a final value of 9.46. Fe-rich olivine(ss) with $X_{Fayalite}$ 0.29 formed near the endpoint
430 and increased rapidly to 3.8 moles before hydrocarbons appeared.
431 The model at 1.5 GPa and 400 °C (Fig. 5B, Table S-2) was similar to the standard model
432 at 2.0 GPa and 400 °C in terms of the mineral sequence, the relative amounts of minerals, and the
433 amount of H_2 reactant. However, the model at 2.0 GPa and 450 °C (Fig. 5C, Table S-3) showed
434 the same mineral sequence as the standard model until magnetite was totally consumed and then
435 olivine(ss) formed before the formation of hydrocarbon fluids. The olivine was Fe-rich ($X_{Fayalite}$
436 0.26), representing a metasomatic composition. It appeared that the breakdown of magnetite
437 caused by the addition of H_2 provided Fe^{2+} that stabilized olivine. If more H_2 was added, olivine
438 became unstable and was reduced to metallic iron. The amount of H_2 (53.9 moles) used here
439 represents the value when 1.0 mole of hydrocarbon formed co-existing with graphite. Graphite
440 was completely destroyed for values of H_2 equal to or more than 66.5 moles.
441 Interestingly, our model at 2.0 GPa and 500 °C (Fig. 5D, Table S-4) contained olivine with
442 antigorite throughout the reaction progress. As magnetite started to decrease sooner in this model,
443 the formation of olivine(ss) was even more strongly favored, and it became the most abundant
444 mineral quickly. When magnetite was destroyed, the iron content of the olivine reached a peak at
445 Fa 21, but then the rate of olivine increase slowed. Forsterite started to increase and finally reached

446 the upper mantle composition (Fo 93). If more H_2 was added, even up to 90.0 moles, no metallic
447 iron formed and the hydrocarbon fluids ended up very H_2-rich. Calcite(ss) was more favored than
448 aragonite at this condition and was reduced to form graphite and then hydrocarbon fluids. Graphite
449 formed only slightly before brucite.

450 In order to investigate the effect of magnetite destruction on the formation of olivine(ss),
451 we tested models without magnetite as a reactant. At 2.0 GPa and 450 °C, without reactant
452 magnetite in the initial rock, we found that only a very small amount of magnetite formed and then
453 disappeared during the run (Fig. 5E). The log number of moles of magnetite was -5.7 to -5.0 during
454 $log\ \xi$ from -3.8 to -2.6. This small amount of magnetite simply reflected the (low) amount of Fe
455 in the initial fluid. No olivine formed. However, for the model at 2.0 GPa and 500 °C also without
456 magnetite, a very small and transient amount of olivine(ss) appeared (Fig. 5F), but at a much later
457 stage of reaction progress than in Fig. 5D at the same pressure and temperature. Only 0.056 moles
458 of olivine(ss) formed from $log\ \xi$ at 0.20 - 0.28 and then disappeared. No extra olivine(ss) formed
459 even if more H_2 was added. The excess H_2 stayed in the hydrocarbon fluids at 2.0 GPa and 500 °C
460 and the hydrocarbon fluids became H_2-rich. Clearly, the absence of magnetite as a reactant had a
461 strong effect in inhibiting olivine(ss) formation at both 450 and 500 °C. We note that in the natural
462 samples, no preserved olivine was observed. The reason for this discrepancy may lie in the highly
463 heterogeneous nature of the Lanzo carbonated serpentinite or to retrograde hydration. If H_2 fluid
464 pathways did not encounter magnetite, or the amount of magnetite encountered was very low, our
465 models show that olivine would not be expected to form to a significant extent.

466 Hydrocarbon fluids formed at the end of the reactions at each pressure and temperature
467 condition are presented in Figs. 5A - F. The final amounts and compositions of the hydrocarbon
468 fluids can be seen in Fig. 6 over the range of 1.0 - 2.0 GPa and 350 - 500 °C. At the higher pressures

and lower temperatures, if olivine(ss) did not form, hydrocarbon fluid formation was favored (Fig. 6A). The reason is simply that the saturation activity of $CH_{4,aq}$ was smaller at higher pressure and lower temperature. In models without magnetite, more hydrocarbons formed, and the degree of increase is greater at higher temperature. Except for the models at 2.0 GPa, 450 °C and 500 °C, the amounts of H_2 were about 66.0 moles. If the saturation activity of $CH^0_{4,aq}$ were smaller (i.e. the solubility was lower), more $CH_{4,f}$ could equilibrate in hydrocarbons.

The fluid compositions shown in Fig. 6B indicate that $CH_{4,f}$ was the most abundant endmember of the immiscible fluids over the temperature range considered. Except at 2.0 GPa and 500 °C, the hydrocarbon was almost pure $CH_{4,f}$ with a mole fraction larger than 0.90. At 2.0 GPa, from 450 °C to 500 °C, the mole fraction of $CH_{4,f}$ dropped from 0.99 to 0.65 as the $H_{2,f}$ component increased up to 0.35. However, other hydrocarbons were negligible. At 1.0 GPa, the mole fraction of $H_{2,f}$ was much greater than at higher pressures at 400 °C. No significant effect on the composition of fluids by pressure was observed. Overall, the fluids were methane-rich without olivine. If more initial H_2 were added, the curves would move towards more H_2-rich compositions. After all the carbon was reduced by the reactant H_2, the $H_{2,f}$ became unreactive and built up as a component in the hydrocarbon fluid.

The final $logf_{O_2}$ at each condition with an F/R equal to 0.1 is given relative to the QFM buffer in Fig 7A. The highest $logf_{O_2}$ was at 2.0 GPa and 450 °C because hydrocarbon fluids formed coexisting with graphite with the lowest initial number of H_2 moles. The $logf_{O_2}$ at 400 °C of both 1.5 and 2.0 GPa were very close, as were the other results for minerals, aqueous species, and hydrocarbon compositions at these conditions. At 2.0 GPa and 350 °C, the $logf_{O_2}$ was lower probably because olivine(ss) was not favored at low temperature and only formed at temperatures

491 greater than 400 °C. The models at 500 °C had the largest initial number of H_2 moles. This large
492 amount of H_2 resulted in the total reduction of oxidized C and the excess H_2 caused extremely
493 reducing conditions (Fig. 7A). The final $logf_{O_2}$ values of the models were not affected
494 significantly by removing magnetite as a reactant.

495 The final pH value of each model (relative to neutral pH) with F/R equal to 0.1 is plotted
496 in Fig. 7B. It can be seen that the final ΔpH values increased less than 0.2 compared to the initial
497 pH values. The fluids are basically Mg-Ca-OH fluids. All of the fluids were alkaline because
498 brucite was in equilibrium with the aqueous fluids, and contributed to Mg^{2+} and OH^-. At 2.0 GPa,
499 the final pH decreased with temperature resulting in less alkaline aqueous fluids. The final Ca
500 concentrations were observed decreasing from 0.038 to 0.021 molal with temperature at 2.0 GPa
501 (Table S1-4). Lower Ca concentrations resulted in lower values of the pH. At 400 °C, the final pH
502 increased from 1.0 to 2.0 GPa. The opposite trend of Ca concentration showed that Ca increased
503 from 0.008 to 0.031 molal with pressure at 400 °C. Interestingly, the drop of pH was affected more
504 by temperature even when Ca decreased by 0.017 molal. Again, the final pH values of the models
505 were not affected by removing magnetite from the reactants.

506 Overall, the above models demonstrated that hydrocarbons could form over a wide range
507 of pressure and temperature conditions, during both the prograde metamorphism and exhumation
508 processes of the Lanzo Massif (Vitale Brovarone *et al.* 2017). The process of hydrocarbon
509 formation was systematically the same as the standard model within the pressure range of 1.5 to
510 2.0 GPa and a temperature range of 400 to 450 °C. The product minerals diopside, brucite, and
511 graphite were consistent with the natural samples at 1.5 to 2.0 GPa. Our model with expanded
512 pressure and temperature conditions predicted small variations of mineral assemblages and
513 hydrocarbon compositions.

514 *4.2.4 Garnet formation*

515 The model results presented above could reproduce with a good confidence level the
516 natural features described by Vitale Brovarone et al. (2017). However, in other samples from the
517 same locality, Giuntoli et al. (2020) also reported the presence of Ca-Fe-rich garnet forming along
518 carbonate reduction channels. The formation of Ca-Fe-rich garnet was not predicted by our models
519 for low carbonate/serpentinite ratios (15 vol.% aragonite; 85 vol.% serpentinite) at 2.0 GPa and
520 400°C provided that we chose an appropriate standard Gibbs free energy of andradite less stable
521 than that reported by Moecher and Chou (1990). However, using the same characterization of
522 andradite, Ca-Fe-rich garnet did form at 2.0 GPa and 400°C when we performed complementary
523 models for two higher carbonate/serpentinite ratios (30 vol.% aragonite, 70 vol.% serpentinite; and
524 50 vol.% aragonite, 50 vol.% serpentinite) consistent with the results described by Giuntoli et al.
525 (2020). In these latter two models, the final mineral assemblage, after antigorite and chlorite were
526 exhausted, brucite, clinopyroxene, aragonite, graphite, and Ca-rich-garnet together with
527 hydrocarbon fluid (see Appendix A).

528 # 5. Discussion

529 ***5.1 Comparison of model results with the altered Lanzo carbonated serpentinites***

530 Our study has established predictive models of the formation of immiscible hydrocarbon
531 fluid during the reaction of H_2 with carbonated serpentinite at temperatures and pressures relevant
532 to subduction zones. Here we compare the model results with the previously reported petrographic
533 results in Vitale Brovarone et al. (2017). As summarized above in Section 2, the overall reaction
534 suggested for the carbonated serpentinite reduction and hydrocarbon formation as in Eq. (1)
535 indicates that antigorite and Ca-carbonate reacted with H_2 to form clinopyroxene, brucite, methane,

and water. The results for our standard model (Fig. 3) agree with this generalized reaction. However, the generalized reaction does not capture all the petrographic detail.

For example, the natural samples contain evidence that Ca-carbonate was first reduced to methane and graphite and then graphite was altered to methane during protracted H_2 infiltration (Vitale Brovarone *et al.* 2017). A recent experimental study is consistent with the proposed latter process (Peña-Alvarez *et al.* 2021). An overall reaction for alteration of Ca-carbonate to graphite was already given in Eqs. (7) and (8). Here we present more detail. In most of our models, Ca-carbonate was first reduced to $CH_{4,aq}$ by H_2, which can be expressed as

$$CaCO_3 + 4H_{2,f} = Ca(OH)^+ + OH^- + CH_{4,aq} + H_2O \quad (10)$$

This reaction contributes to the early increases in pH and $CH^0_{4,aq}$ seen in Figs. 3D and E. The $logf_{O_2}$ continued to decrease and $a_{CH_{4,aq}}$ increased to reach the equilibrium between $CH^0_{4,aq}$ and graphite, coexisting with the reactant Ca-carbonate, which can be expressed by

$$CH^0_{4,aq} + CaCO_3 = 2C^{graphite} + Ca(OH)^+ + OH^- + H_2O \quad (11)$$

During the co-existence of aragonite and graphite, $logf_{O_2}$ was buffered (Fig. 3D). But with even more H_2 reacting, eventually the aragonite was completely destroyed and the $logf_{O_2}$ dropped associated with an increase in the $a_{CH^0_{4,aq}}$. In turn, these changes destabilized graphite in favor of CH_4-rich fluid according to Eq. (9) above. In this way, the model predicted the formation of graphite from aragonite, and subsequently the formation of immiscible hydrocarbon fluid from graphite. The model prediction is therefore in agreement with the data for the natural samples with regard to an important sequence of events.

Another way to compare the model results with the natural samples is to examine the fluid chemistry. The fluid inclusions reported for the altered carbonated serpentinite (Section 2) were

mostly CH_4-H_2-rich (plus minor ethane), associated with graphite rims on serpentinite clasts. Minor amounts of H_2O-bearing inclusions were related to graphite-free serpentinite clasts. The first type is approximated by our model immiscible hydrocarbon fluid. At 2.0 GPa and 400 °C, the model fluid is predominantly CH_4 with minor H_2 and very minor amounts of ethane as the second most abundant hydrocarbon. Despite the approximations in our model regarding ideal solution in the hydrocarbon fluid, the above results are reasonably consistent with the actual fluid inclusions. The H_2O-bearing fluid inclusions associated with graphite-free partially reacted carbonated serpentinites, could represent an early stage in our models with higher $logf_{O_2}$ and lower $a_{CH^0_{4,aq}}$.

5.2 Carbon and Hydrogen budget during hydrocarbon formation

In all our models, the carbon in the initial system is almost entirely present in the carbonated serpentinites as a carbonate mineral. In the standard model at 2.0 GPa and 400 °C, when hydrocarbon fluid first appeared at $log\ \xi$ of 1.61, the carbon budget in moles was 76.5%, 0.2%, and 23.3% of graphite, hydrocarbon, and aqueous carbon, respectively. Graphite then dropped to only 9.3%, whereas hydrocarbons increased to 67.5%, and aqueous carbon remained about the same. In the final step, the hydrocarbon fluid contained 77.1% and aqueous carbon contained 22.9% of the total carbon.

The budget of hydrogen (H) is also important because H from the influx of $H_{2,f}$ can be incorporated into antigorite and brucite, as well as aqueous and hydrocarbon fluids. The H in the initial system before $H_{2,f}$ reacted was almost all in antigorite and the initial water. The mole percentages were 49.6 % and 50.4 %, respectively.

However, the final hydrogen budget (Table 3) shows that H_2O still took up nearly half of the H even after 66.5 moles of $H_{2,f}$ were added to the system. A lot of H_2O formed during the

580 reactions and brucite was the second most abundant species containing 17.7% of the total H.
581 Antigorite contained only 14.1%. Methane in the hydrocarbon fluid constituted 14.4% of the total
582 hydrogen, but $CH_{4,aq}$ constituted only 4.2% of the total hydrogen. Compared with the carbon
583 budget, the hydrogen budget was more complex because multiple types of H-bearing species
584 existed in models at all temperature-pressure conditions, and were not affected by the carbon
585 mineral sequences, although the percentages varied. Overall, both the carbon and hydrogen
586 budgets were useful tools for tracking the redox reactions systematically.

587 ***5.3 Origin of H_2 fluids that reacted with carbonated serpentinites in the Lanzo Massif***

588 The origin of the large amounts of H_2 fluid involved in the alteration of the Lanzo
589 carbonated serpentinties is an interesting topic. It has been suggested that the H_2 could have
590 originated by serpentinization of the fresh peridotite rocks in the massif during subduction and
591 then migrated along channelized fluid pathways (Debret *et al.* 2013, Vitale Brovarone *et al.* 2017,
592 2020). Typically, H_2 can be generated by the oxidation of the fayalite endmember in primary
593 peridotitic olivine, which can be expressed as

594 $$3Fe_2SiO_4 + 2H_2O \rightarrow 2Fe_3O_4 + 3SiO_{2,aq} + 2H_2 \quad (11)$$

595 The above reaction enables an estimate of the amount of olivine that would need to be
596 serpentinized to provide all the H_2 for making CH_4. For example, at 2.0 GPa and 400 °C, 66.5
597 moles of $H_{2,f}$ were needed to form 12.7 moles of $CH_{4,f}$. According to Eq. (11), 99.75 moles of
598 fayalite would be needed. If we assume that the mole fraction of fayalite in the peridotitic olivine
599 was 7%, then 1,325 moles of forsterite should be serpentinized. Using the following
600 serpentinization reaction

601 $$34Mg_2SiO_4 + 51H_2O \rightarrow Mg_{48}Si_{34}O_{85}(OH)_{62} + 20Mg(OH)_2 \quad (12)$$

602 the 1,325 moles of forsterite should produce 39 moles of antigorite. Overall, to form 66.5 moles
603 of $H_{2,f}$ (around 903 cm^3) and 12.7 moles of $CH_{4,f}$, about 0.06 m^3 of olivine were destroyed and
604 about 0.07 m^3 of antigorite were created These quantities of minerals are small compared to the
605 amounts available in a massif.

606 CH_4-H_2-rich fluid inclusions have also been found in the high-pressure serpentinized
607 ultramafic peridotites of other subduction zone complexes (Vitale Brovarone *et al.* 2020, Boutier
608 *et al.* 2021). Additional reduced fluid species such as H_2S and NH_3 were found in some of the
609 preserved inclusions. The condition of high-pressure serpentinization happened near the peak
610 metamorphic condition, 370 - 400 °C and 1 GPa for the eclogitic-facies Lanzo massif. Graphitic
611 carbon was not commonly observed, which was consistent with our model at those temperature
612 and pressure conditions (Fig. 5A). The $log\ f_{O_2}$ of serpentinization was inferred to be less than
613 QFM because awaruite was associated with antigorite. CH_4 in the fluid inclusions was thought to
614 have been formed by reduction of carbon in the serpentinizing fluid.

615 ## 6. Conclusions

616 We have focused on predicting the formation of immiscible hydrocarbon fluids at upper
617 mantle conditions. We set up initial aqueous speciation and solubility models in equilibrium with
618 carbonated serpentinite consistent with the natural samples reported by Vitale Brovarone et al.
619 (2017) and Giuntoli et al. (2020). The initial fluids were then used in chemical mass transfer
620 models simulating the irreversible reactions during the reduction of carbonated serpentinites by
621 invading H_2 fluids. Immiscible hydrocarbon fluids formed in association with major changes of
622 mineralogy and aqueous solution chemistry. The models covered a pressure-temperature range of
623 1.0 - 2.0 GPa and 350 - 500 °C.

We found the following principal results from this modeling study:

- Chemical mass transfer models predicted minerals and hydrocarbon fluids consistent with field and laboratory observations in Vitale Brovarone et al. (2017) and Giuntoli et al. (2020):

  a) Serpentinite (antigorite, magnetite, and chlorite) and aragonite were destroyed.

  b) Brucite, clinopyroxene(ss), graphite, and immiscible hydrocarbon fluids were formed at 1.5 and 2.0 GPa and 400 - 500 °C.

  c) For high initial carbonate/serpentinite ratios, Ca-Fe-rich garnet was formed at 400°C and 2.0 GPa.

  d) Methane was the main constituent of the immiscible hydrocarbon fluids and also reached molal concentrations in the coexisting aqueous fluids.

- As an example, the reaction progress during our standard run at 2.0 GPa and 400 °C with F/R mass ratio of 0.10 revealed the sequence of mineral formation, the number of moles and volumes of each mineral, the aqueous fluid composition and speciation, and the evolution of the $logf_{O_2}$ and pH. During the reactions, aragonite was reduced by H_2 to form graphite and then graphite was reduced to hydrocarbon fluid (almost pure $CH_{4,f}$) associated with an almost continuous drop of $logf_{O_2}$.
- The reaction of H_2 with carbonated serpentinite generated significant amounts of H_2O.
- Lower F/R (aqueous fluid/rock) ratios imply more H_2 fluids, which resulted in greater amounts of H_2O and hydrocarbon fluids formed.
- At 1.0 GPa and 400 °C, graphite was not stable due to the $\log(a_{Ca^{2+}}/a_{H^+}^2)$ of the system being too low.

- Even small amounts of magnetite in the initial rock caused olivine(ss) to appear before hydrocarbon formation in models at 1.0 GPa and 400 °C, 2.0 GPa and 450 °C, and 2.0 GPa and 500 °C. Olivine was not stable if the reactant carbonated serpentinite did not contain magnetite.
- Carbon and hydrogen budgets trace the transfer and redistribution of these elements during the redox reactions.
- Overall, the combined results of the modeling study and the natural samples strongly support the concept that CH_4-rich immiscible hydrocarbon fluids have formed at eclogite facies conditions in subduction zones. How widespread this phenomenon is (at the present and in the geologic past) remains to be seen.

Data Availability:

The files of the model results are available on Johns Hopkins Research Data Repository using the DOI given below. The data can be referred to using the citation below.

Huang, Jingyi; Sverjensky, Dimitri A.; Daniel, Isabelle; Brovarone, Alberto Vitale, 2022, "Data associated with: Reaction path model of the formation of abiotic immiscible hydrocarbon fluids in subducted carbonated serpentinites, Lanzo Massif (Western Italian Alps)", https://doi.org/10.7281/T1/NLHSKE, *Johns Hopkins Research Data Repository*.

Acknowledgements:

This research was supported by a Johns Hopkins Graduate Fellowship, the NSF Grant #2032039, and DOE Grant #DE-SC0019830. This work is part of a project that has received

667 funding from the European Research Council (ERC) under the European Union's Horizon 2020
668 research and innovation programme (Grant agreement No. 864045). This work also received
669 support by the Richard Lounsbery foundation. We would like to thank Daniel Viete for reading a
670 version of this manuscript. We gratefully acknowledge the help and support of the Johns Hopkins
671 University. We thank Fang Huang and Zhigang Zhang for discussions.

672 ## Appendix A. Supplementary Material

673 The supplementary material contains the description of model files and tables about the
674 summary of the initial and final fluid compositions and mineral assemblages. The files contain
675 model results of H_2 fluid reacting with carbonated serpentinites with 15 vol% of aragonite and 85
676 vol% of serpentinite at 2.0 GPa and 400 °C, 1.0 GPa and 400 °C, 1.5 GPa and 400 °C, 2.0 GPa
677 and 450 °C, and 2.0 GPa and 500 °C; with 30 vol% of aragonite and 70 vol% of serpentinite at
678 400°C and 2.0 GPa; and with 50 vol% of aragonite and 50 vol% of serpentinite at 400°C and 2.0
679 GPa.
680

References:

Alt, J.C., Schwarzenbach, E.M., Früh-Green, G.L., Shanks, W.C., Bernasconi, S.M., Garrido, C.J., Crispini, L., Gaggero, L., Padrón-Navarta, J.A., and Marchesi, C., 2013. The role of serpentinites in cycling of carbon and sulfur: Seafloor serpentinization and subduction metamorphism. Lithos, 178, 40–54.

Barbier, S., Huang, F., Andreani, M., Tao, R., Hao, J., Eleish, A., Prabhu, A., Minhas, O., Fontaine, K., Fox, P., and Daniel, I., 2020. A Review of H2, CH4, and Hydrocarbon Formation in Experimental Serpentinization Using Network Analysis. Frontiers in Earth Science, 8 (June), 1–20.

Berman, R.G., 1988. Internally-Consistent Thermodynamic Data for Minerals in the System Na2O-K2O-CaO-MgO-FeO-Fe2O3-Al2O3-SiO2-TiO2-H2O-CO2. Journal of Petrology, 29 (2), 445–522.

Boutier, A., Vitale Brovarone, A., Martinez, I., Sissmann, O., and Mana, S., 2021. High-pressure serpentinization and abiotic methane formation in metaperidotite from the Appalachian subduction, northern Vermont. Lithos, 396–397, 106190.

Dasgupta, R. and Hirschmann, M.M., 2010. The deep carbon cycle and melting in Earth's interior. Earth and Planetary Science Letters, 298, 1–13.

Debret, B., Nicollet, C., Andreani, M., Schwartz, S., and Godard, M., 2013. Three steps of serpentinization in an eclogitized oceanic serpentinization front (Lanzo Massif - Western Alps). Journal of Metamorphic Geology, 31 (2), 165–186.

Foustoukos, D.I. and Stern, J.C., 2012. Oxidation pathways for formic acid under low temperature hydrothermal conditions: Implications for the chemical and isotopic evolution of organics on Mars. Geochimica et Cosmochimica Acta, 76, 14–28.

Giuntoli, F., Vitale Brovarone, A., and Menegon, L., 2020. Feedback between high-pressure genesis of abiotic methane and strain localization in subducted carbonate rocks. Scientific Reports, 10 (1), 1–15.

Gold, T., 1992. The deep, hot biosphere. Proceedings of the National Academy of Sciences of the United States of America, 89 (13), 6045–6049.

Gold, T., 2001. The deep hot biosphere: the myth of fossil fuels. Springer Science & Business Media.

Hacker, B.R., Abers, G.A., and Peacock, S.M., 2003. Subduction factory 1. Theoretical mineralogy, densities, seismic wave speeds, and H 2 O contents. Journal of Geophysical Research: Solid Earth, 108 (B1).

Holt, A.F. and Condit, C.B., 2021. Slab Temperature Evolution Over the Lifetime of a Subduction Zone. Geochemistry, Geophysics, Geosystems, 22 (6).

Huang, F., Daniel, I., Cardon, H., Montagnac, G., and Sverjensky, Di.A., 2017. Immiscible hydrocarbon fluids in the deep carbon cycle. Nature Communications, 8 (May).

Huang, F. and Sverjensky, D.A., 2019. Extended Deep Earth Water Model for predicting major element mantle metasomatism. Geochimica et Cosmochimica Acta, 254, 192–230.

Huang, J., Daniel, I., Sverjensky, D.A., Cardon, H., and Montagnac, G., 2023. Formation of hydrocarbons favored by high pressure at subduction zone conditions. Chemical Geology, 630, 121489.

723 Van Keken, P.E., Kiefer, B., and Peacock, S.M., 2002. High-resolution models of subduction
724 zones: Implications for mineral dehydration reactions and the transport of water into the
725 deep mantle. Geochemistry, Geophysics, Geosystems, 3 (10).
726 Klein, F., Grozeva, N.G., and Seewald, J.S., 2019. Abiotic methane synthesis and
727 serpentinization in olivine-hosted fluid inclusions. Proceedings of the National Academy of
728 Sciences of the United States of America, 116 (36), 17666–17672.
729 Kolesnikov, A., Kutcherov, V.G., and Goncharov, A.F., 2009. Methane-derived hydrocarbons
730 produced under upper-mantle conditions. Nature Geoscience, 2 (8), 566–570.
731 Kolesnikov, A.Y., Saul, J.M., and Kutcherov, V.G., 2017. Chemistry of Hydrocarbons Under
732 Extreme Thermobaric Conditions. ChemistrySelect, 2 (4), 1336–1352.
733 Kudryavtsev, N., 1951. Against the organic hypothesis of the origin of petroleum. Neftianoye
734 Khozyaistvo, 9, 17–29.
735 Kudryavtsev, N.A., 1959. Geological proof of the deep origin of petroleum. Trudy Vsesoyuz.
736 Neftyan. Nauch. Issledovatel Geologoraz Vedoch. Inst, 132, 242–262.
737 Kutcherov, V.G. and Krayushkin, V.A., 2010. Deep-seated abiogenic origin of petroleum: From
738 geological assessment to physical theory. Reviews of Geophysics, 48 (1), 1–30.
739 Lagabrielle, Y., Fudral, S., and Kienast, J.-R., 1990. La couverture océanique des ultrabasites de
740 Lanzo (Alpes occidentales): arguments lithostratigraphiques et pétrologiques. Geodinamica
741 Acta, 4 (1), 43–55.
742 Li, Y., 2017. Immiscible CHO fluids formed at subduction zone conditions. Geochem. Pespect.
743 Lett, 3, 12–21.
744 Manning, C.E., Shock, E.L., and Sverjensky, D.A., 2013. The chemistry of carbon in aqueous
745 fluids at crustal and upper-mantle conditions: Experimental and theoretical constraints.
746 Reviews in Mineralogy and Geochemistry, 75, 109–148.
747 McCollom, T.M., 2013. Laboratory simulations of abiotic hydrocarbon formation in earth's deep
748 subsurface. Reviews in Mineralogy and Geochemistry, 75, 467–494.
749 McDermott, J.M., Seewald, J.S., German, C.R., and Sylva, S.P., 2015. Pathways for abiotic
750 organic synthesis at submarine hydrothermal fields. Proceedings of the National Academy
751 of Sciences of the United States of America, 112 (25), 7668–7672.
752 Mendeleev, D., 1877. L'origine du petrole. Revue Scientifique, 2e Ser. (VIII), 409–416.
753 Moecher, D.P. and Chou, I.-M., 1990. Experimental investigation of andradite and hedenbergite
754 equilibria employing the hydrogen sensor technique, with revised estimates of Delta Gf 0
755 (sub m,298) for andradite and hedenbergite. American Mineralogist, 75 (11–12), 1327–
756 1341.
757 Pelletier, L. and Müntener, O., 2006. High-pressure metamorphism of the Lanzo peridotite and
758 its oceanic cover, and some consequences for the Sesia-Lanzo zone (northwestern Italian
759 Alps). Lithos, 90 (1–2), 111–130.
760 Peña-Alvarez, M., Brovarone, A.V., Donnelly, M.E., Wang, M., Dalladay-Simpson, P., Howie,
761 R., and Gregoryanz, E., 2021. In-situ abiogenic methane synthesis from diamond and
762 graphite under geologically relevant conditions. Nature Communications, 12 (1).
763 Penniston-Dorland, S.C., Kohn, M.J., and Manning, C.E., 2015. The global range of subduction
764 zone thermal structures from exhumed blueschists and eclogites: Rocks are hotter than
765 models. Earth and Planetary Science Letters, 428, 243–254.

766 Piccoli, F., Rubatto, D., Ovtcharova, M., Hermann, J., Guillong, M., and Vitale Brovarone, A.,
767 2023. Dating fluid infiltration and deformation in the subducted ultramafic oceanic
768 lithosphere by perovskite geochronology. Chemical Geology, 615.
769 Proskurowski, G., Lilley, M.D., Seewald, J.S., Früh-Green, G.L., Olson, E.J., Lupton, J.E.,
770 Sylva, S.P., and Kelley, D.S., 2008. Abiogenic hydrocarbon production at lost city
771 hydrothermal field. Science, 319 (5863), 604–607.
772 Pruteanu, C.G., Ackland, G.J., Poon, W.C.K., and Loveday, J.S., 2017. When immiscible
773 becomes miscible-Methane in water at high pressures.
774 Reeves, E.P. and Fiebig, J., 2020. Abiotic synthesis of methane and organic compounds in
775 earth's lithosphere. Elements, 16 (1), 25–31.
776 Rubatto, D. and Hermann, J., 2001. Exhumation as fast as subduction? Geology, 29 (1), 3–6.
777 Scambelluri, M., Cannaò, E., and Gilio, M., 2019. The water and fluid-mobile element cycles
778 during serpentinite subduction. A review. European Journal of Mineralogy, 31 (3), 405–
779 428.
780 Sephton, M.A. and Hazen, R.M., 2013. On the origins of deep hydrocarbons. Reviews in
781 Mineralogy and Geochemistry, 75, 449–465.
782 Sverjensky, D., Daniel, I., and Brovarone, A.V., 2020. The Changing Character of Carbon in
783 Fluids with Pressure: Organic Geochemistry of Earth's Upper Mantle Fluids. In:
784 Geophysical Monograph Series. John Wiley and Sons Inc, 259–269.
785 Sverjensky, D.A., 2019. Thermodynamic modelling of fluids from surficial to mantle conditions.
786 Journal of the Geological Society, 176 (2), 348–374.
787 Sverjensky, D.A., Harrison, B., and Azzolini, D., 2014. Water in the deep Earth: The dielectric
788 constant and the solubilities of quartz and corundum to 60kb and 1200°C. Geochimica et
789 Cosmochimica Acta, 129, 125–145.
790 Sverjensky, D.A., Hemley, J.J., and D'angelo, W.M., 1991. Thermodynamic assessment of
791 hydrothermal alkali feldspar-mica-aluminosilicate equilibria. Geochimica et Cosmochimica
792 Acta, 55 (4), 989–1004.
793 Syracuse, E.M., van Keken, P.E., Abers, G.A., Suetsugu, D., Bina, C., Inoue, T., Wiens, D., and
794 Jellinek, M., 2010. The global range of subduction zone thermal models. Physics of the
795 Earth and Planetary Interiors, 183 (1–2), 73–90.
796 Tao, R., Zhang, L., Tian, M., Zhu, J., Liu, X., Liu, J., Höfer, H.E., Stagno, V., and Fei, Y., 2018.
797 Formation of abiotic hydrocarbon from reduction of carbonate in subduction zones:
798 Constraints from petrological observation and experimental simulation. Geochimica et
799 Cosmochimica Acta, 239, 390–408.
800 Vitale Brovarone, A., Martinez, I., Elmaleh, A., Compagnoni, R., Chaduteau, C., Ferraris, C.,
801 and Esteve, I., 2017. Massive production of abiotic methane during subduction evidenced in
802 metamorphosed ophicarbonates from the Italian Alps. Nature Communications, 8, 1–13.
803 Vitale Brovarone, A., Sverjensky, D.A., Piccoli, F., Ressico, F., Giovannelli, D., and Daniel, I.,
804 2020. Subduction hides high-pressure sources of energy that may feed the deep subsurface
805 biosphere. Nature Communications, 11 (1), 1–11.
806 Wolery, T.J., 1992. EQ3/6, a software package for geochemical modeling of aqueous systems:
807 Package overview and installation guide (Version 7.0).
808 Zhang, C. and Duan, Z., 2010. GFluid: An Excel spreadsheet for investigating C-O-H fluid
809 composition under high temperatures and pressures. Computers and Geosciences, 36 (4),
810 569–572.

Zhu, J., Zhang, L., Tao, R., and Fei, Y., 2020. The formation of graphite-rich eclogite vein in S.W. Tianshan (China) and its implication for deep carbon cycling in subduction zone. Chemical Geology, 533.

A.

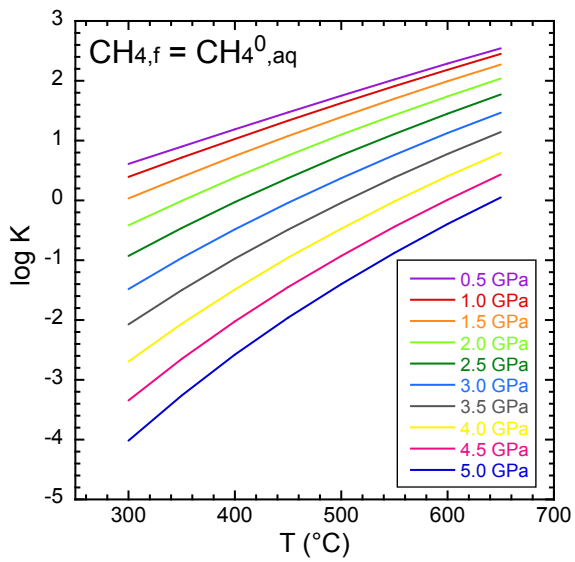

B.

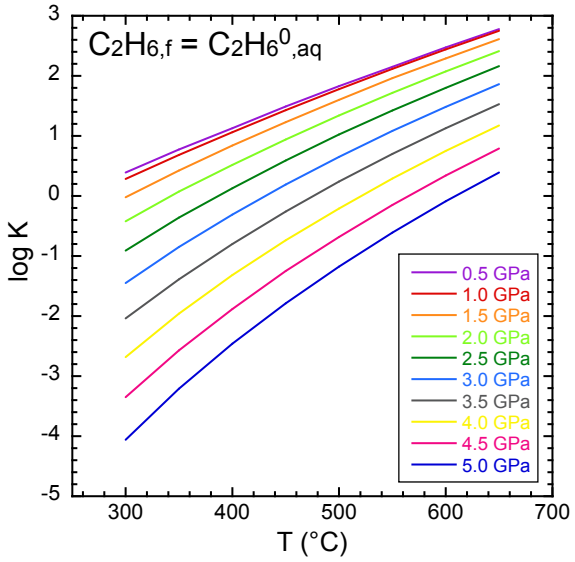

C.

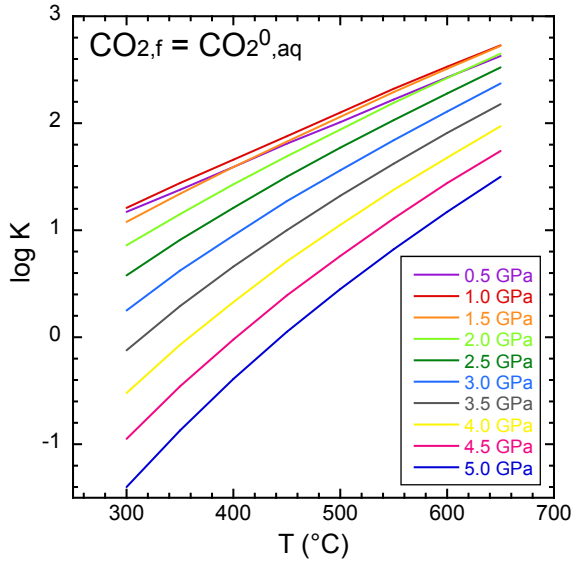

D.

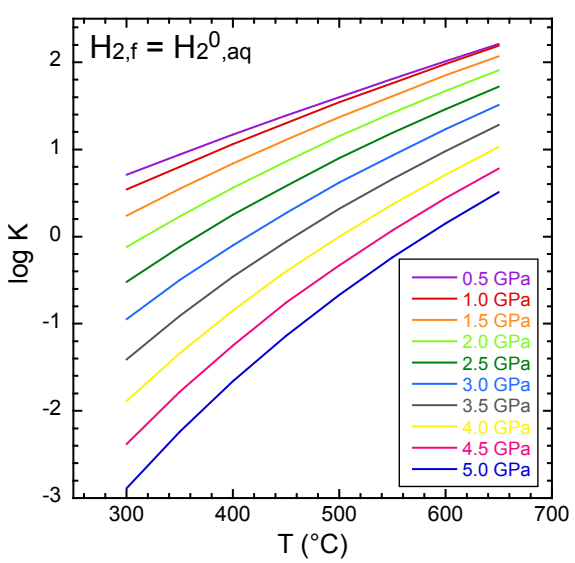

Figure 1. *Log K* of reactions of fluid species and aqueous species. **(A)** CH_4, **(B)** C_2H_6, **(C)** CO_2, and **(D)** H_2.

A.

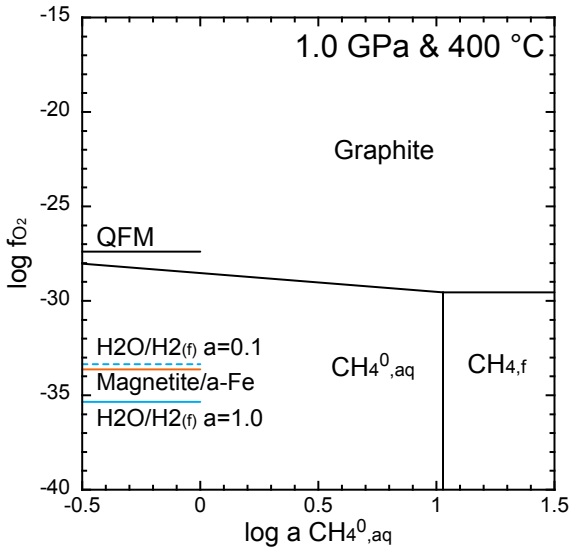

B.

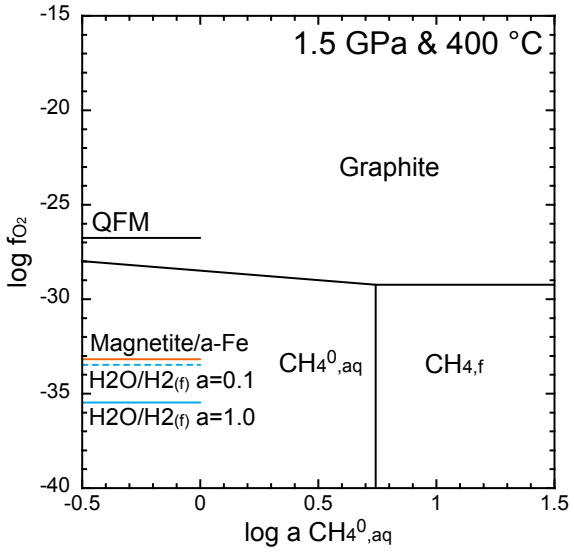

C.

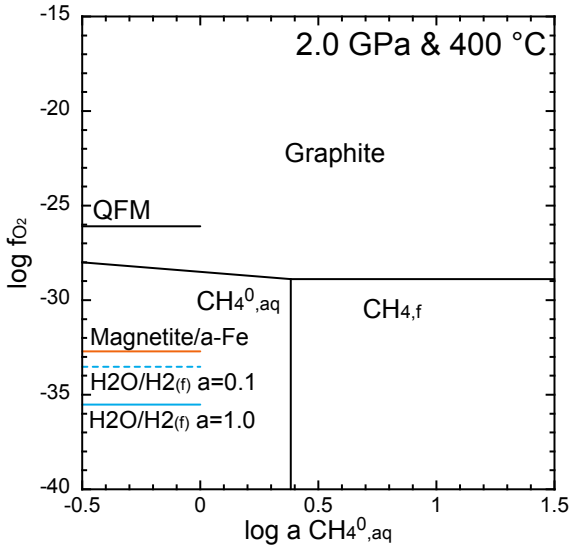

D.

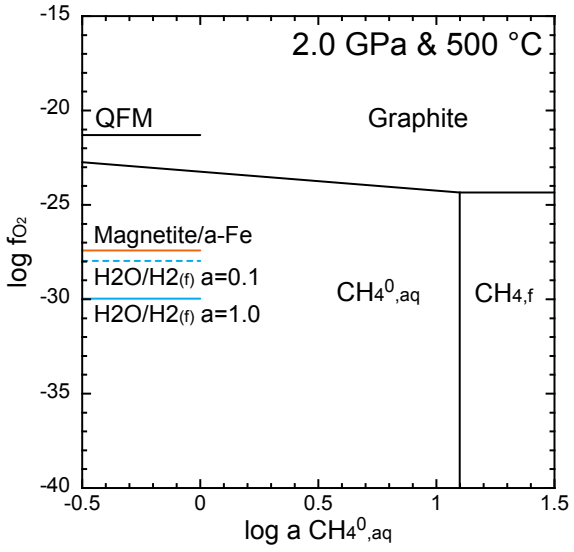

Figure 2. $Logf_{O_2}$ vs. $loga_{CH^0_{4,aq}}$ diagrams of the stability field among graphite, $CH^0_{4,aq}$, and $CH_{4,f}$ at **(A)** 1.0 GPa & 400 °C, **(B)** 1.5 GPa & 400 °C, **(C)** 2.0 GPa & 400 °C, and **(D)** 2.0 GPa & 500 °C.

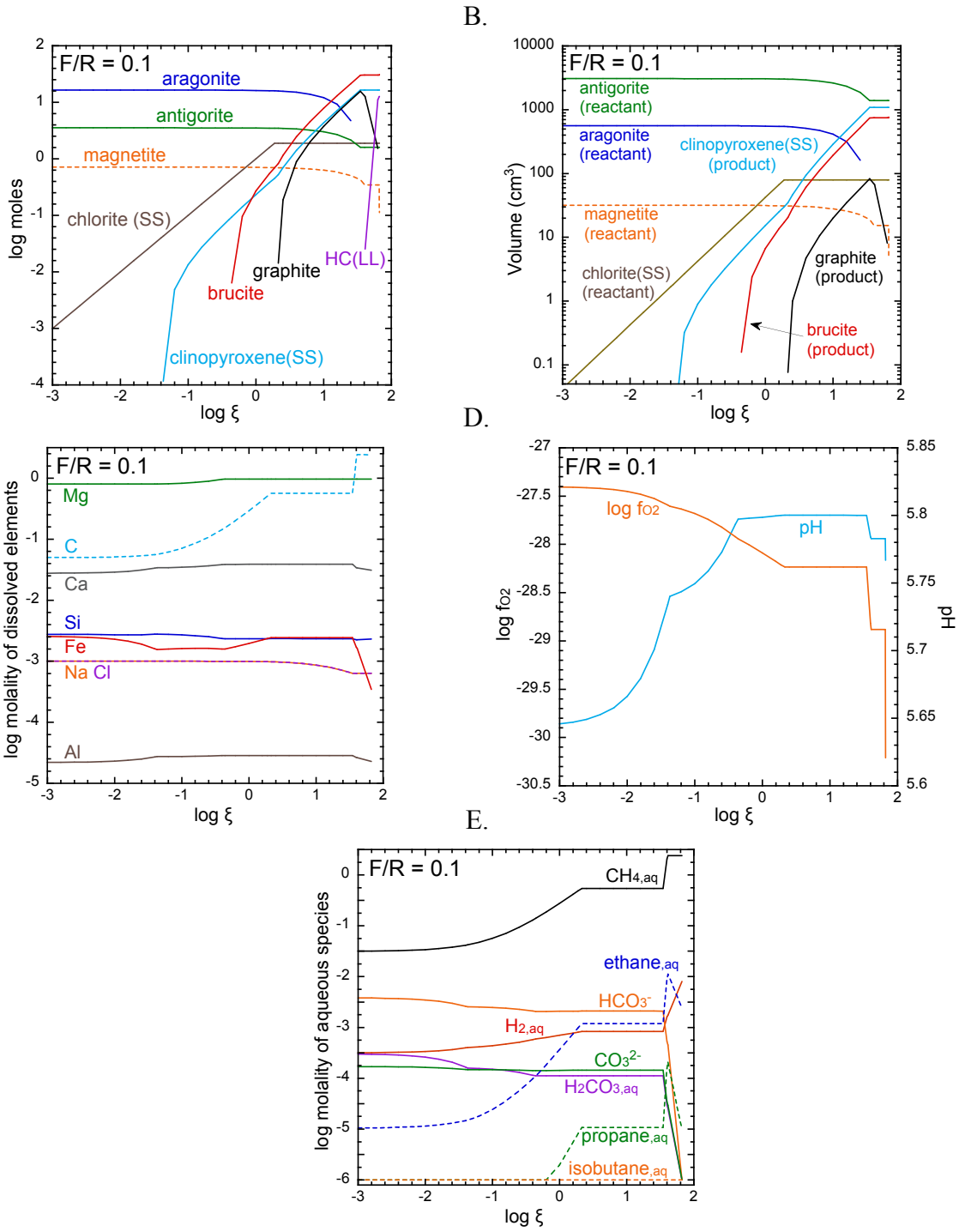

Figure 3. Reaction path model of the reduction of carbonated serpentinite by H_2 at 2.0 GPa and 400.0 °C with F/R equal to 0.1 (by weight) as a function of the logarithm of the reaction progress ($log\ \xi$): **(A)** minerals and hydrocarbon fluid, **(B)** volumes of minerals, **(C)** dissolved elements, **(D)** $logf_{O_2}$ and pH, and **(E)** aqueous species.

A.

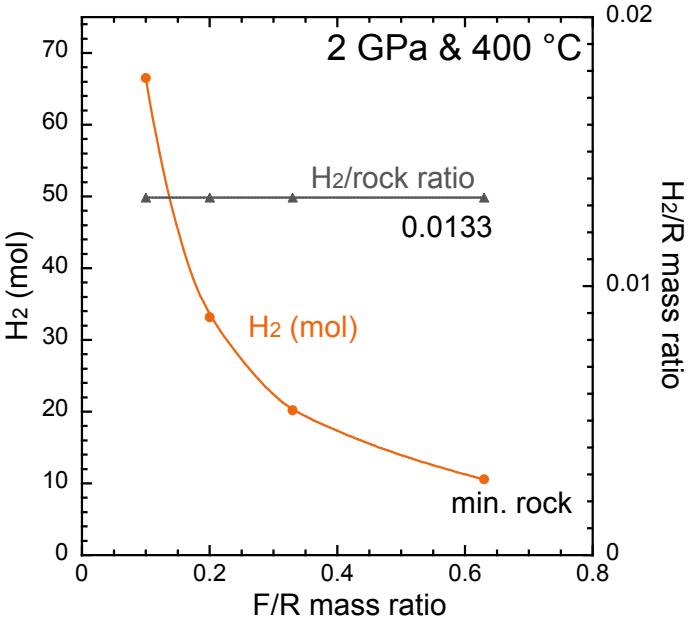

B.

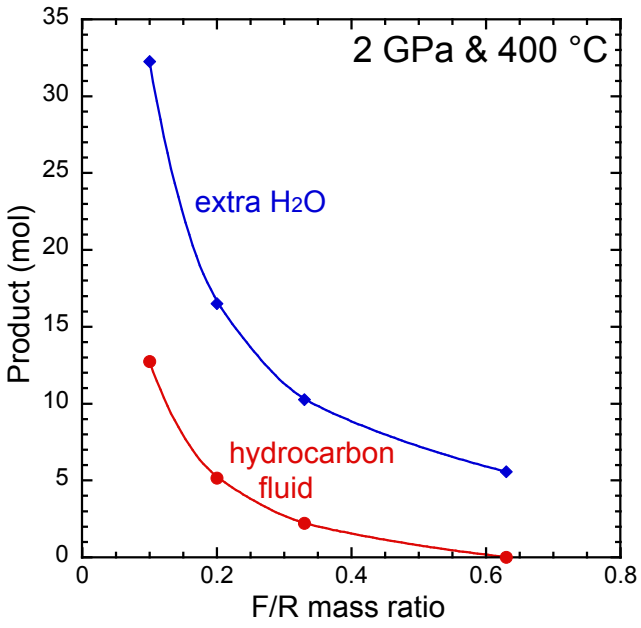

Figure 4. (A) Number of moles of H_2 consumed and the H_2/R mass ratio vs. F/R mass ratio; **(B)** Number of moles of immiscible hydrocarbon fluids and excess H_2O formed vs. F/R mass ratio.

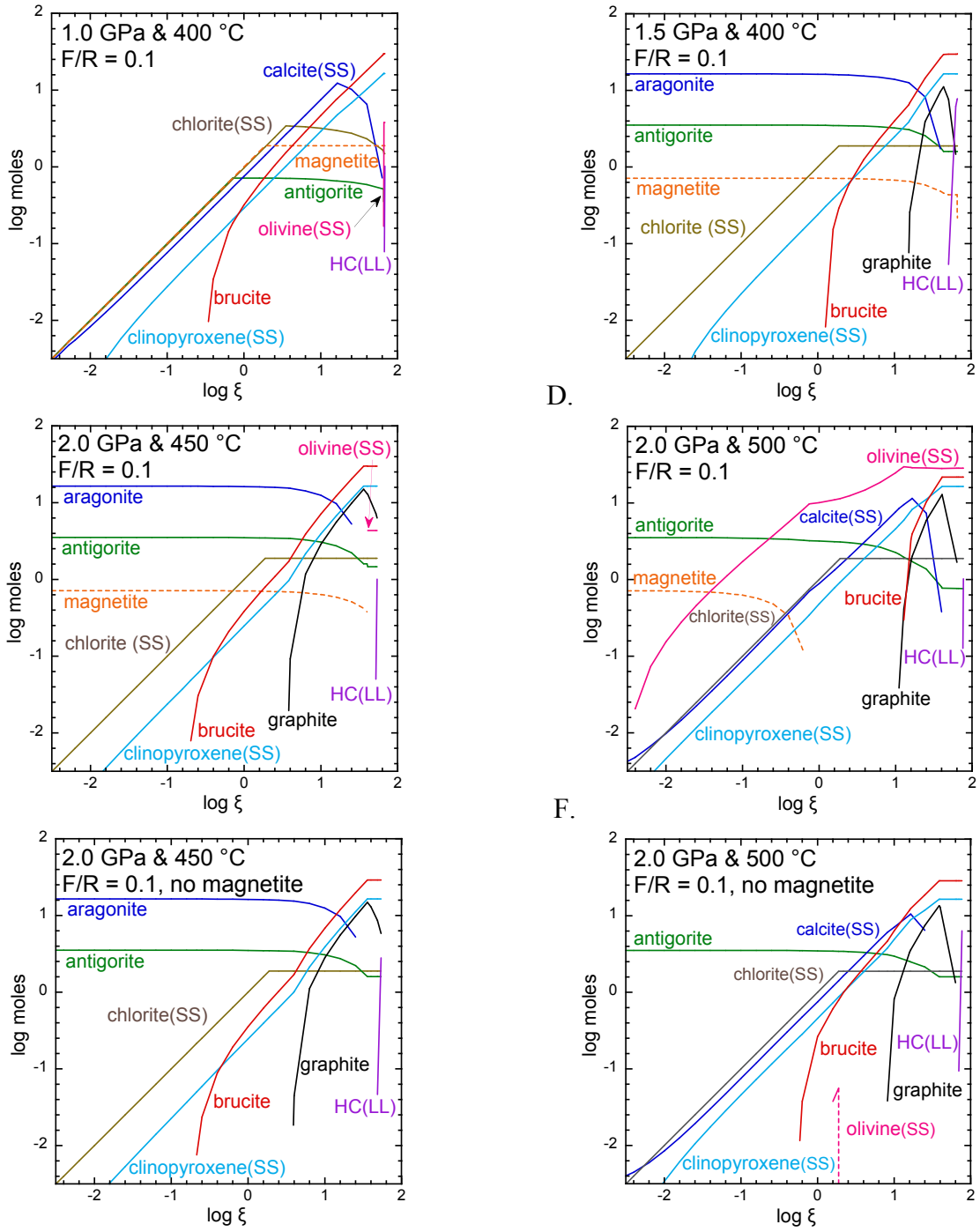

Figure 5. Reaction path models of the destruction of carbonated serpentinites by H_2 at different temperatures and pressures with F/R equal to 0.1 (by weight). The logarithms of the number of moles of minerals produced are shown as functions of $log\ \xi$: **(A)** 1.0 GPa and 400 °C; **(B)** 1.5 GPa and 400 °C; 2.0 GPa and **(C)** 450 °C, **(D)** 500 °C; 2.0 GPa and **(E)** 450 °C, (F) 500 °C GPa without initial reactant magnetite.

A.

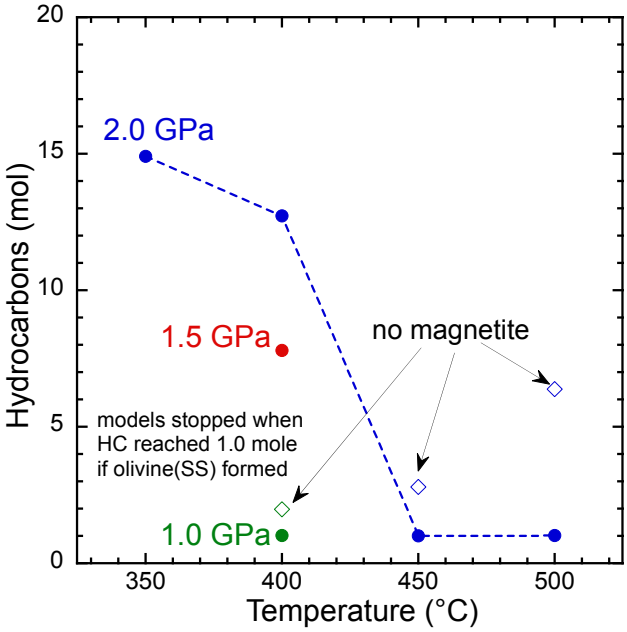

B.

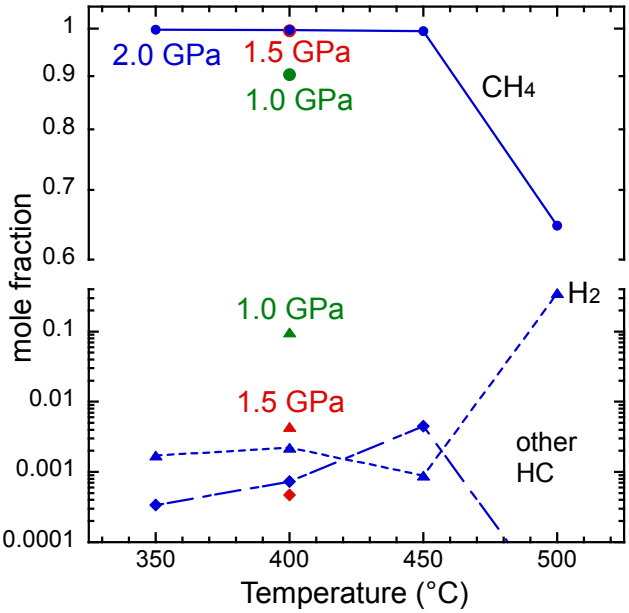

Figure 6. (A) Number of moles of hydrocarbon fluids and **(B)** mole fractions of fluid hydrocarbon species vs. temperature at 1.0 (green), 1.5 (red), and 2.0 (blue) GPa. **(A)** Models without magnetite are represented by empty diamonds. **(B)** The dots and solid line represent CH_4, the triangles and dashed line represent H_2, and the diamonds and dash-dotted line represent other hydrocarbons (see text).

A.

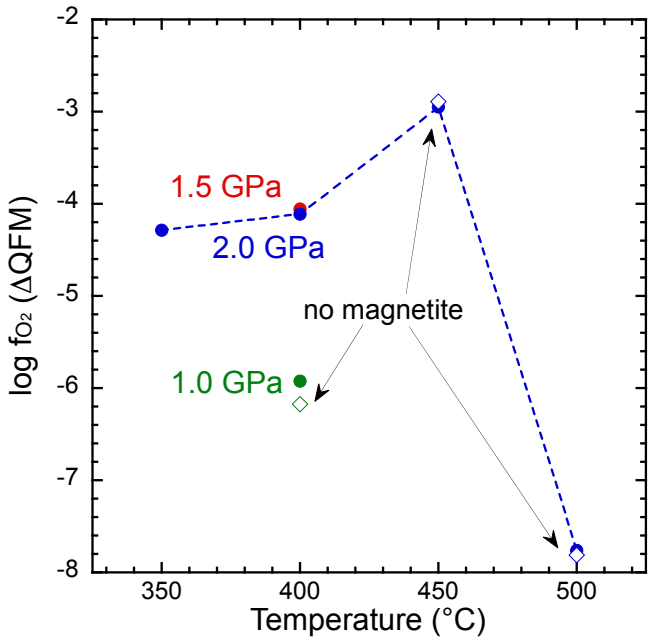

B.

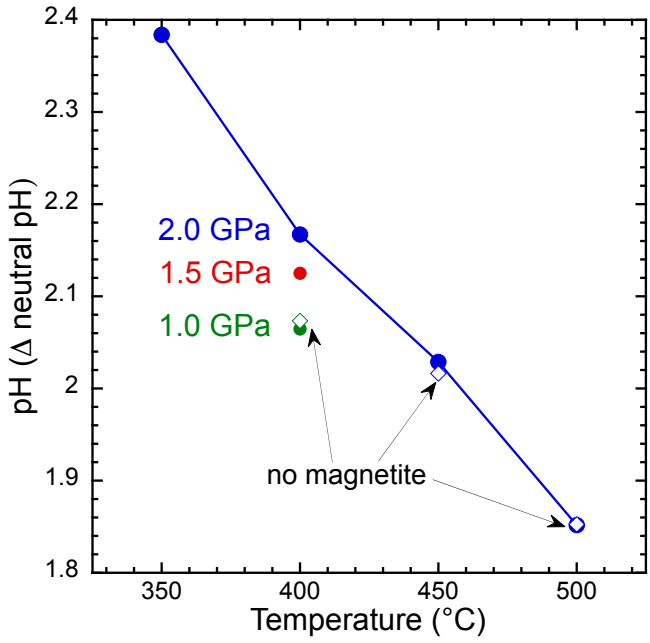

Figure 7. (A) $Log\ f_{O_2}$ relative to QFM and **(B)** pH relative to neutral pH vs. temperature at the end of the reactions with F/R 0.1 at 1.0 GPa (green), 1.5 GPa (red), and 2.0 GPa (blue). Models without magnetite are represented by empty diamonds.

Table 1. Summary of the initial and final fluid compositions and mineral assemblages at 400 °C and 2.0 GPa with F/R 0.1. Full details of the aqueous speciation of all the elements at each step of the reaction progress are given in the reaction path output file (see File 1 in Appendix A).

INITIAL	Parameter		FINAL	Parameter
FLUID	value[a.]		FLUID	value[a.]
Na	0.001		Na	0.0006
Mg	0.8		Mg	0.969
Ca	0.028		Ca	0.031
Fe	0.003		Fe	0.001
Al	0.00002		Al	0.00002
Si	0.003		Si	0.002
Cl	0.001		Cl	0.0006
C	0.05		C	2.413
$CH_{4,aq}$	0.0314		$CH_{4,aq}$	2.408
HCO_3^-	0.0038		HCO_3^-	9e-7
$Ca(HCO_3)^+$	0.0067		$Ca(HCO_3)^+$	2e-6
CO_3^{2-}	0.0002		CO_3^{2-}	6e-8
$CaCO_{3,aq}$	0.0013		$CaCO_{3,aq}$	6e-7
$H_2CO_{3,aq}$	0.0003		$H_2CO_{3,aq}$	6e-8
$CO_{2,aq}$	0.0004		$CO_{2,aq}$	8e-8
$HCOO^-$	0.0011		$HCOO^-$	7e-6
$Fe(HCOO)^+$	0.0024		$Fe(HCOO)^+$	0.00005
$Ca(HCOO)^+$	0.0016		$Ca(HCOO)^+$	0.00001
pH	5.64		pH	5.77
Neutral pH	3.60		Neutral pH	3.60
$logf_{O_2}$	-27.4		$logf_{O_2}$	-30.2
ΔQFM	-1.3		ΔQFM	-4.1
REACTANT MINERALS	COMPONENTS	REACTANT MOLE FRACTION	FINAL PRODUCT MOLE FRACTION	FINAL PRODUCT MOLES
ARAGONITE	$CaCO_3$	1.0	n.d.	0.0
ANTIGORITE	$Mg_{24}Si_{17}O_{73.5}H_{31}$	1.0	1.0	1.598
MAGNETITE	Fe_3O_4	1.0	1.0	0.113
CHLORITE	Clinochlore	0.97	0.90	1.696
	Chamosite	0.03	0.10	0.188
PRODUCT MINERALS	COMPONENTS			
CLINOPYROXENE	Diopside	n.d.	0.90	14.786
	Hedenbergite	n.d.	0.10	1.643
	Jadeite	n.d.	0.0	0.0
BRUCITE	$Mg(OH)_2$	n.d.	1.0	31.053
GRAPHITE	C	n.d.	n.d.	0.0

[a.] Concentrations given in molality (m).

Table 2. The amounts of initial reactant H_2, and the initial and final rock and fluid-rock (F/R) mass ratios, as well as the final excess of H_2O created and the amounts of immiscible hydrocarbon fluid created.

Reactants				Final			
F/R	M_R [a]	N_{H_2} [b]	H_2/R [c]	$M_R{}'$ [a]	F/R'	Extra N_{H_2O} [d]	N_{HC} [e]
0.10	10.0	66.5	0.0133	9.27	0.17	32.3	12.7
0.20	5.00	33.2	0.0133	4.63	0.28	16.5	5.15
0.33	3.03	20.2	0.0133	2.81	0.42	10.3	2.20
0.63	1.59	10.6	0.0133	1.46	0.75	5.57	0.012

[a] mass of rock in kg, [b] moles of H_2, [c] mass ratio of H_2 and rock, [d]Excess moles of water created relative to the initial 55.51 moles, [e] moles of hydrocarbon fluid created.

Table 3. The final hydrogen budget (mole of element percentage) of the model at 2.0 GPa & 400 °C with F/R 0.1.

Mineral		Aqueous fluid		Hydrocarbon fluid	
antigorite	14.1%	$CH_{4,aq}$	4.2%	$CH_{4,f}$	14.4%
brucite	17.7%	H_2O	49.6%		
chlorite	<1%	$Mg(OH)_2$	<1%		